AMERICAN SOCIETY FOR MICROBIOLOGY | Journal of Bacteriology®

RESEARCH ARTICLE

In Situ Structure of the *Vibrio* Polar Flagellum Reveals a Distinct Outer Membrane Complex and Its Specific Interaction with the Stator

Shiwei Zhu,[a,b]* Tatsuro Nishikino,[c] Norihiro Takekawa,[d] Hiroyuki Terashima,[c] Seiji Kojima,[c] Katsumi Imada,[d] Michio Homma,[c] Jun Liu[a,b]

[a]Department of Microbial Pathogenesis, Yale University School of Medicine, New Haven, Connecticut, USA
[b]Microbial Sciences Institute, Yale University, West Haven, Connecticut, USA
[c]Division of Biological Science, Graduate School of Science, Nagoya University, Nagoya, Japan
[d]Department of Macromolecular Science, Graduate School of Science, Osaka University, Toyonaka, Osaka, Japan

ABSTRACT The bacterial flagellum is a biological nanomachine that rotates to allow bacteria to swim. For flagellar rotation, torque is generated by interactions between a rotor and a stator. The stator, which is composed of MotA and MotB subunit proteins in the membrane, is thought to bind to the peptidoglycan (PG) layer, which anchors the stator around the rotor. Detailed information on the stator and its interactions with the rotor remains unclear. Here, we deployed cryo-electron tomography and genetic analysis to characterize *in situ* structure of the bacterial flagellar motor in *Vibrio alginolyticus*, which is best known for its polar sheathed flagellum and high-speed rotation. We determined *in situ* structure of the motor at unprecedented resolution and revealed the unique protein-protein interactions among *Vibrio*-specific features, namely the H ring and T ring. Specifically, the H ring is composed of 26 copies of FlgT and FlgO, and the T ring consists of 26 copies of a MotX-MotY heterodimer. We revealed for the first time a specific interaction between the T ring and the stator PomB subunit, providing direct evidence that the stator unit undergoes a large conformational change from a compact form to an extended form. The T ring facilitates the recruitment of the extended stator units for the high-speed motility in *Vibrio* species.

IMPORTANCE The torque of flagellar rotation is generated by interactions between a rotor and a stator; however, detailed structural information is lacking. Here, we utilized cryo-electron tomography and advanced imaging analysis to obtain a high-resolution *in situ* flagellar basal body structure in *Vibrio alginolyticus*, which is a Gram-negative marine bacterium. Our high-resolution motor structure not only revealed detailed protein-protein interactions among unique *Vibrio*-specific features, the T ring and H ring, but also provided the first structural evidence that the T ring interacts directly with the periplasmic domain of the stator. Docking atomic structures of key components into the *in situ* motor map allowed us to visualize the pseudoatomic architecture of the polar sheathed flagellum in *Vibrio* spp. and provides novel insight into its assembly and function.

KEYWORDS bacterial flagellar motor, cryo-electron tomography, flagellar outer membrane complex, nanomachine, protein-protein interactions

Many bacteria swim in liquid environments or swarm on surfaces. Flagella are the main organelles responsible for bacterial motility. Flagellar structure and function have been well studied using peritrichous flagella of *Salmonella* spp. and *Escherichia coli*. The flagellum is composed of three distinct parts, the filament, the hook, and the

Citation Zhu S, Nishikino T, Takekawa N, Terashima H, Kojima S, Imada K, Homma M, Liu J. 2020. *In situ* structure of the *Vibrio* polar flagellum reveals a distinct outer membrane complex and its specific interaction with the stator. J Bacteriol 202:e00592-19. https://doi.org/10.1128/JB.00592-19.

Editor Ann M. Stock, Rutgers University-Robert Wood Johnson Medical School

Address correspondence to Michio Homma, g44416a@cc.nagoya-u.ac.jp, or Jun Liu, jliu@yale.edu.

* Present address: Shiwei Zhu, Howard Hughes Medical Institute, Yale University School of Medicine, New Haven, Connecticut, USA.

Received 22 September 2019
Accepted 18 November 2019
Accepted manuscript posted online 25 November 2019
Published 29 January 2020

basal body (1, 2). The basal body functions as a reversible rotary motor composed of a rotor and several stator units. The rotor, which penetrates both inner and outer membranes, consists of a bushing, a rod, an MS ring, and a C ring. The bushing is made up of the P ring at the peptidoglycan (PG) layer and the L ring at the outer membrane. The structure made by the rings corresponding to the outer membrane is called the flagellar outer membrane complex (FOMC). The basal body functions as a reversible rotary motor with several stator units. The stator has an ion-conducting activity, and torque is generated via changes in interactions between the rotor and the stator units that that are induced by ion flow through the stator. *In vivo* studies using stators labeled with fluorescent protein demonstrated that the stator units dynamically assemble into or disassemble from an active motor (3, 4). The ion conduction of the stator is activated after the stator units are arranged and anchored around the rotor. The stator unit is a heterohexamer of four A subunits and two B subunits, for example, MotA and MotB for *E. coli* and PomA and PomB for *Vibrio*. The B subunit has a conserved PG binding motif in its periplasmic OmpA-like domain. Thus, the stator unit is believed to be bound to the PG layer (5–7), but the mechanisms of the stator anchoring and the channel activation are still obscure.

Many bacterial pathogens, including *Vibrio*, *Pseudomonas*, *Campylobacter*, and *Helicobacter* species, are equipped with a polar flagellum. Recent structural studies of polar flagella have revealed that they are often equipped with extra ring-like structures, which are not present in the peritrichous flagella, surrounding the L and P rings (8–11), although their shapes and sizes vary between species (12, 13). Among bacteria with polar flagella, *Vibrio alginolyticus* is a model organism to investigate both structure and function of the sheathed polar flagellum (14, 15).

The *Vibrio* flagellar basal body has two *Vibrio*-specific features around the P ring, the H ring and the T ring. The T ring is located beneath the P ring and is composed of MotX and MotY (16, 17). MotY forms the main body of the T ring, while MotX is likely located in the edge of the T ring. The T ring is known for its essential role in torque generation and recruitment of the *Vibrio* stator unit, which is composed of four PomA and two PomB subunits (16). MotX is suggested to interact with the periplasmic region of PomB ($PomB_C$) (18), while MotY interacts with the basal body (17), presumably at the L/P rings. The stator is believed to be bound to the T ring through the interaction between MotX and the periplasmic domain of PomB. The H ring is a large ring-like structure surrounding the bushing and extends along the periplasmic face of the outer membrane. The H ring is composed of FlgT, FlgP, and FlgO (12, 19, 20). FlgT stabilizes the T ring and is important for torque generation (19, 21). FlgT and FlgO are required for the flagellar penetration of the outer membrane (20). Thus, the H ring is important for flagellar formation and bacterial motility.

Recent structural studies using cryo-electron tomography (cryo-ET) have revealed the *in situ* architecture of the flagellar motor (22). The location of each component protein in the H and T rings has been determined using various deletion mutants (9, 20). The density corresponding to the T ring shows a clear 13-fold symmetry (9). The inner membrane-spanning densities around the rotor also have 13-fold symmetry, suggesting that these densities correspond to the stators (12). However, the exact location of the stator B subunit (PomB) and its interaction with the rotor are still unknown. For further understanding of the flagellar assembly process, including the incorporation and activation of the stator, high-resolution *in situ* structures will be required.

Here, we analyzed *in situ* structures of the polar flagellar motor of *V. alginolyticus* by combining time-resolved cryo-ET with genetic analysis. Subtomogram averaging enabled us to determine a higher-resolution structure and build a molecular model of the *Vibrio* flagellar motor. We showed for the first time how the T ring interacts with the H ring and recruits stator units. We also revealed key intermediates in polar flagellar assembly. Altogether, our study provides novel insights into flagellar motor assembly and function in *V. alginolyticus*.

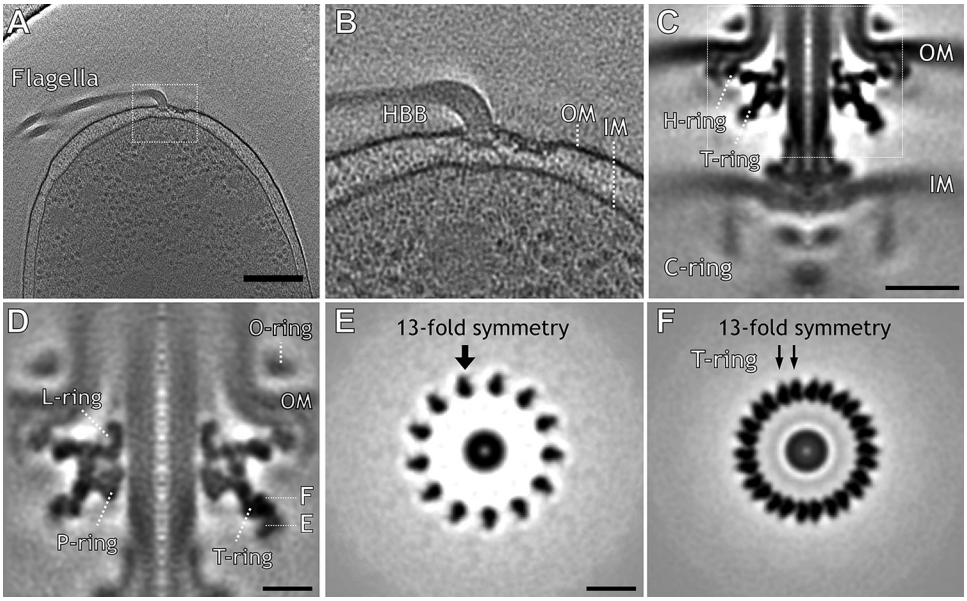

FIG 1 *In situ Vibrio* flagellar motor revealed by cryo-electron tomography together with the Volta phase plate. *In situ Vibrio alginolyticus* flagellar motor structure obtained by cryo-ET. (A) Representative tomographic slice of a three-dimensional (3D) reconstruction of strain KK148 showing cellular features in good contrast. (B) Zoomed-in view shows the flagellar motor embedded in the outer membrane (OM) and inner membrane (IM). (C) Central slice from a subtomogram average of the intact flagellar motor shows the H ring, T ring, and C ring. (D) A central slice of the focused refined structure shows the T ring surrounding the L ring and P ring, which form the bushing part of the flagellar motor. (E) Cross-section shows a novel ring with13-fold symmetry. (F) Another cross-section shows the T ring with 26-fold symmetry. Bars, 200 nm (A), 20 nm (C), and 10 nm (D and E).

RESULTS

High-resolution *in situ* motor structure of the *Vibrio* sheathed flagellum. We collected several hundred cryo-ET tomograms from cells of an *flhG* mutant (KK148) in which multiple polar flagella are commonly found in cell poles (Fig. 1A and B). A total of 3,020 subtomograms of flagellar motors were used to generate a high-resolution *in situ* structure of the intact motor (Fig. 1C). Focused refinement was used to determine a higher-resolution structure of the flagellar outer membrane complex (FOMC) (Fig. 1D to F). There are 13 pairs of protrusions bridged by a globular density surrounding the P ring. The 26 protrusions correspond to the T ring and attach to the densities of H and P rings (Fig. 1D and F). The cross-section around the tip of the T ring shows globular densities with 13-fold rotational symmetry (Fig. 1E).

Molecular architecture of the H and T rings in FOMC. To better understand the FOMC structure in three dimensions, we took advantage of recent characterization of the H and T rings (9, 12, 19–21) and crystal structures of FlgT and MotY, which are the major components of the H and T rings, respectively (17, 19) (Fig. 2). The H ring is likely composed of FlgO, FlgP, and FlgT (20). The *in situ* location of each protein is described in Fig. S1 in the supplemental material according to previous and present cryo-ET results from deletion mutants. FlgO is located in the outermost region of the H ring (20), and FlgP is in the middle region of the H ring (12). FlgT is believed to form the innermost region of the H ring (19–21). Indeed, 26 copies of the crystal structure of FlgT fit well into the averaged cryo-ET map (Fig. 2D). FlgT is composed of three domains, an N-terminal domain (FlgT-N), a middle domain (FlgT-M), and a C-terminal domain (FlgT-C). FlgT-N is located near the L ring, and FlgT-M is adjacent to the P ring (19). As FlgT-N has highly positively and negatively charged regions, their interactions between two neighboring subunits appear to facilitate the formation of the innermost part of the H ring (Fig. 2D). Importantly, the FlgT ring model is consistent with our previous observation that FlgT-N contributes to the formation of the H ring. FlgT-M stabilizes the T ring and interacts with the basal body (19).

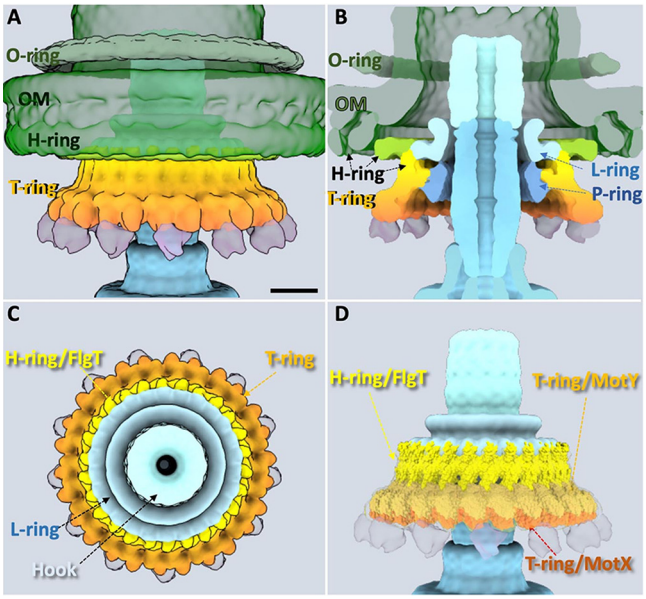

FIG 2 Molecular architecture of *Vibrio*-specific T/H rings. (A) Three-dimensional surface rendering of the top parts of *Vibrio* flagellar basal body, including the O ring, outer membrane (OM), H ring, and T ring. (B) Clipped view of panel A shows the L ring and the P ring in addition to the O ring, H ring, and T ring. The location of the H-ring components is clarified based on the results from the current FlgT mutant and the previous results. FlgO is labeled in deep green and located at the distal area of the H ring; FlgP is labeled in light green and located in the middle area of the H ring. FlgT might directly locate outside the P/L rings and on the top of the T ring. (C) A top view of panel A after removing the sheath and O ring shows the hook, L ring, H ring, and T ring. An additional ring-like density underneath the T ring is shown in a transparent purple. (D) Atomic models of FlgT, MotY, and MotX are docked into the cryo-ET density map based on the 26-fold symmetry structure we solved (see Materials and Methods). Bar, 10 nm.

MotY is the main component of the T ring, and MotX is located in the edge of the T ring (9, 16). The crystal structure of MotY consists of the N-terminal domain (MotY-N), which interacts with MotX, and the C-terminal domain (MotY-C), which contains a peptidoglycan binding motif (17). Twenty-six copies of the crystal structure of MotY fit well into the T-ring density (Fig. 2D and Fig. S2). In this model, the putative peptidoglycan binding site of MotY-C faces to the peptidoglycan layer (Fig. S3) and is adjacent to the FlgT-M domain, and MotY-N is located at the periphery of the T ring to interact with MotX. Although the structure of MotX has not been determined, MotX has a characteristic SEL1 repeat, a structural motif consisting of a repeat of α-helices that is involved in protein-protein interaction, in its sequence (23). We built a putative structure model of MotX *in silico* and fitted it in the protrusion density. From this work, we determined the molecular architecture of the T ring, which is composed of 26 copies of the MotX-MotY heterodimer.

Interaction between the stator and the T ring. Twenty-six copies of the MotX-MotY heterodimer fit well into the T-ring density (Fig. 2), enabling us to clearly see the extra densities with 13-fold symmetry (Fig. 1E and 2B and D). As MotX is known to interact with the stator unit, we therefore speculate that the extra densities are formed by part of the stator units. To test our hypothesis, we determined the motor structure of the Δ*pomA* Δ*pomB* mutant and compared it with the wild-type (WT) motor structure (Fig. 3). The globular density (black arrow in Fig. 3A) at the periphery of the T ring is absent (arrow in Fig. 3B), suggesting that it is likely formed by the periplasmic domain of the stator unit.

A functional stator unit is composed of four PomA and two PomB subunits (24). PomB has a large periplasmic domain, whereas PomA has a cytoplasmic domain. The crystal structure of the C-terminal periplasmic domain of the PomB ($PomB_C$) dimer (6) fits well into the globular density adjacent to the T ring (Fig. 3C to F). The structural model revealed that each subunit of the $PomB_C$ dimer directly interacts with MotX of

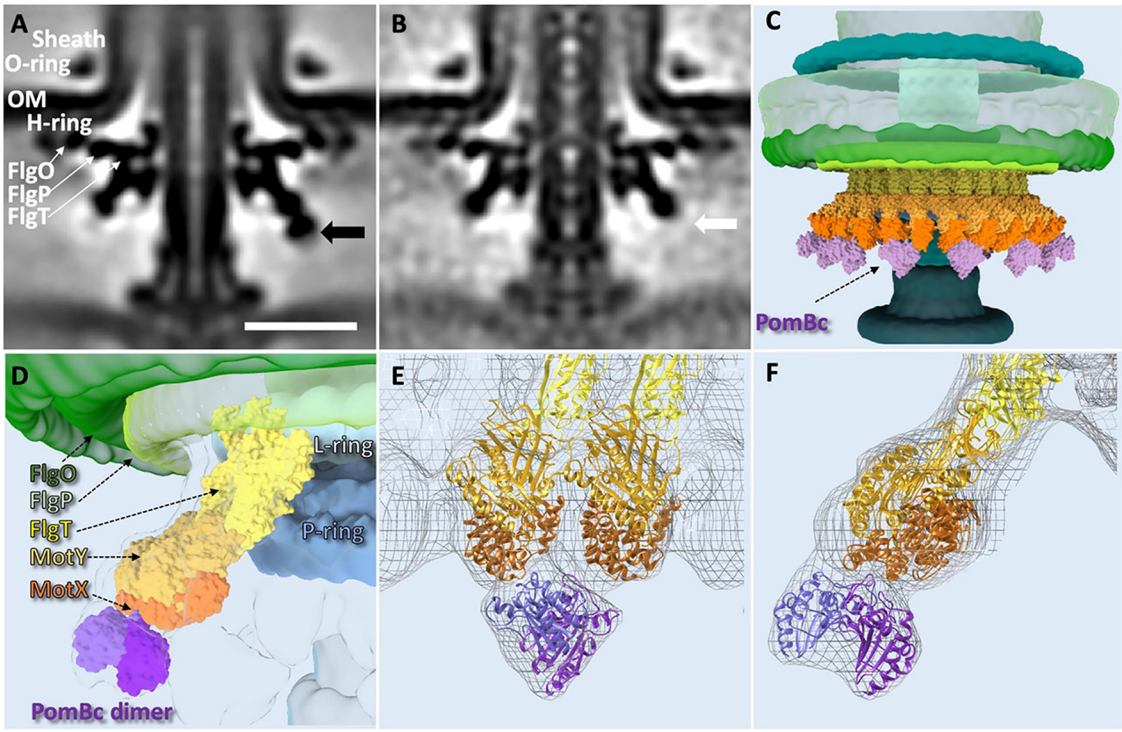

FIG 3 Identification of stator B subunit location and binding sites. (A) Two-dimensional (2D) slice of subtomogram-averaged structure of the top part of the *Vibrio* motor in the KK148 strain. The components of the H ring have been labeled as FlgO, FlgP, and FlgT. The black arrow shows an additional/uncharacterized density beneath the T ring. OM, outer membrane. (B) A 2D slice view of the averaged structure of the top part of the *Vibrio* motor in KK148 Δ*pomAB*. The region indicated by the arrow shows the loss of density beneath the T ring, suggesting that the cryo-ET density beneath the T ring is derived from the PomB protein. (C) The atomic structure of $PomB_{C5}$ was fitted into the 13 cryo-ET densities (purple) beneath the T ring. (D) Zoomed-in view shows a stator B unit within the dimer directly interacting via a PG-binding site with 2 units of MotX located at the bottom of the T ring. (E, F) Superimposition of the cryo-ET density map (mesh) and the atomic models of FlgT, MotY, MotX, and PomB. The models are shown as ribbon diagrams and colored as in panel D.

the T ring through the putative peptidoglycan binding site, which includes the β2-α3 loop and the β3-α4 loop (Fig. S2). This peptidoglycan binding site of $PomB_C$ is fully covered by the T ring density. Thus, our structure suggests that the *Vibrio* stator unit is anchored to the T ring instead of to the PG layer. Furthermore, the distance between the inner membrane and the periplasmic domain is about 15 nm, indicating that the intact stator unit is about 20 nm in length from the top of the C ring to the bottom of the T ring. It is considerably longer than the purified stator unit, which was believed to adopt a compact conformation (25). The cryo-ET data are, however, consistent with our previous model in that a large conformational change in the N-terminal region of $PomB_C$ is required for anchoring the stator unit around the rotor (6).

The rotor is required for the interaction between the stator and the T ring. To further validate our model that the stator-rotor interaction may trigger the conformational change of the stator unit to facilitate stator-T ring interaction, we specifically analyzed the FOMCs that lack the MS ring and the rod, as they were commonly found in various gammaproteobacteria (10, 26), including *Pseudomonas aeruginosa* and *V. alginolyticus* (Fig. 1B). Cryo-ET analysis of the Δ*flgO*, Δ*motY* mutants, and WT cells (Fig. 4) confirmed that the FOMCs are indeed composed of the H, T, L, and P rings. However, there is no $PomB_C$ binding to the T ring, indicating that there is no direct stator-T ring interaction in the absence of the MS ring and the rod. Therefore, we conclude that the stator-rotor interaction triggers the stator conformational change from a compact form to an extended form, as we proposed previously (27), which enables the specific interaction between $PomB_C$ and MotX and the recruitment of the stator units around the T ring. In addition, FOMC is rarely assembled without a flagellar rod. We found 137

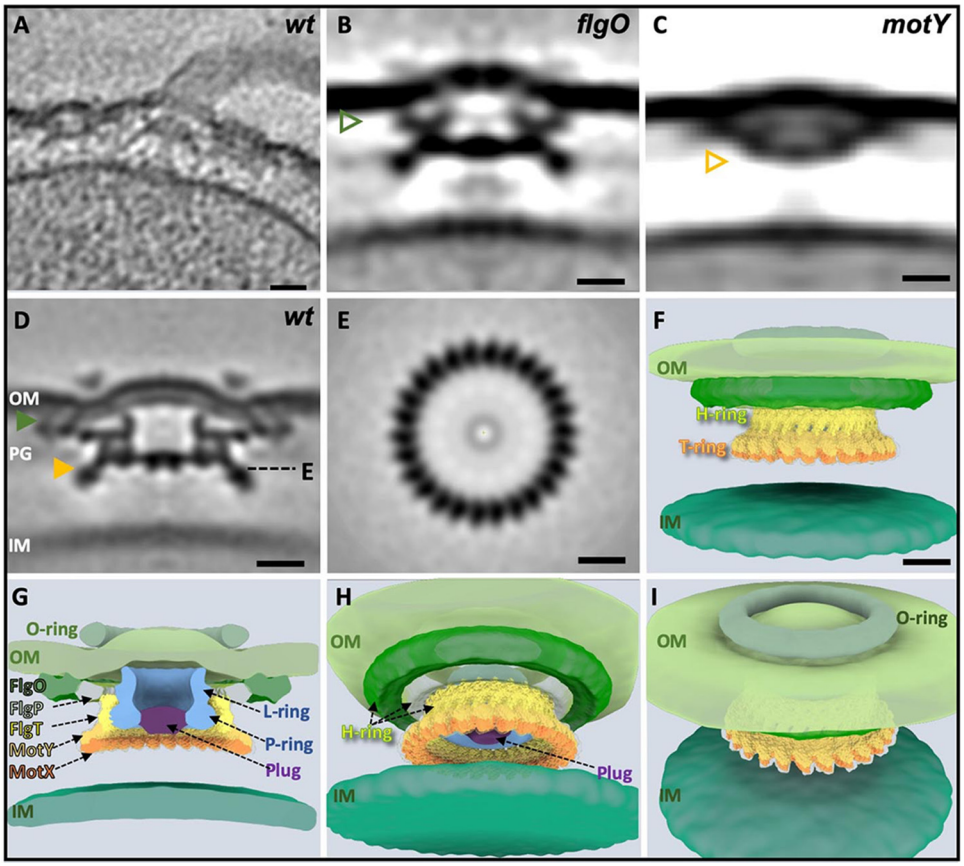

FIG 4 The flagellar outer membrane complex (FOMC) is composed of *Vibrio* T/H/O rings in addition to P/L rings. (A) Representative slice of a tomogram from KK148 wild type (*wt*). (B) An averaged structure of FOMC from the Δ*flgO* mutant. The triangle indicates that the density on the distal area of the H ring is not visible due to absence of the FlgO protein. (C) Averaged structure of the FOMC from the Δ*motY* mutant. The triangle indicates that the density of the T ring is lost due to deletion of the MotY protein. (D) Averaged structure of FOMC from KK148 (*wt*). The FlgO of the H ring is labeled with a green triangle; the T ring is labeled with a yellow triangle. (E) Cross-section view of the T-ring bottom. (F) A 3D surface rendering of the FOMC from KK148. The crystal structures of FlgT, MotY, and MotX are well fitted into both the H and T rings. (G) Central-cut view of the structure shown in panel F showing that, in addition to the T/H rings and the O ring, FOMC has P/L rings, together with a plug located inside the P ring. (H) A −30° tilting view of the structure shown in panel F around the *x* axis, which shows that the plug is located inside the P ring. (I) A 30° tilting view of the structure shown in panel F around the *x* axis reveals a smaller O ring sealed with the outer membrane. IM, inner membrane; OM, outer membrane. Bars, 10 nm.

inner membrane complexes that include the MS/C rings, but only four FOMCs from the 271 particles picked from various rod mutants (Table 1). Thus, FOMC is not a product of flagellar assembly but is a nonfunctional product that might come from flagellar disassembly (26).

Time-coursed cryo-ET captures key intermediates of polar flagellar assembly. To further understand the assembly process of the polar flagellum, we performed cryo-ET analysis of the *Vibrio* cells in various growth stages. We observed the cells in the lag phase or the early stage of the log phase in order to capture the initial and

TABLE 1 Observed flagellar basal body numbers in the rod dysfunction mutants

Strain genotype	No. of[a]:				
	Tilt series	Tomograms	IMCs	FOMCs	No. of IMCs + FOMCs
Δ$flgB_C$	13	11	32	0	32
Δ$flgC_C$	82	72	49	4	53
Δ$flgG_N$	23	9	23	0	23
Δ$flgF_C$	63	49	33	0	33

[a]IMC, inner membrane complex; FOMC, flagellar outer membrane complex.

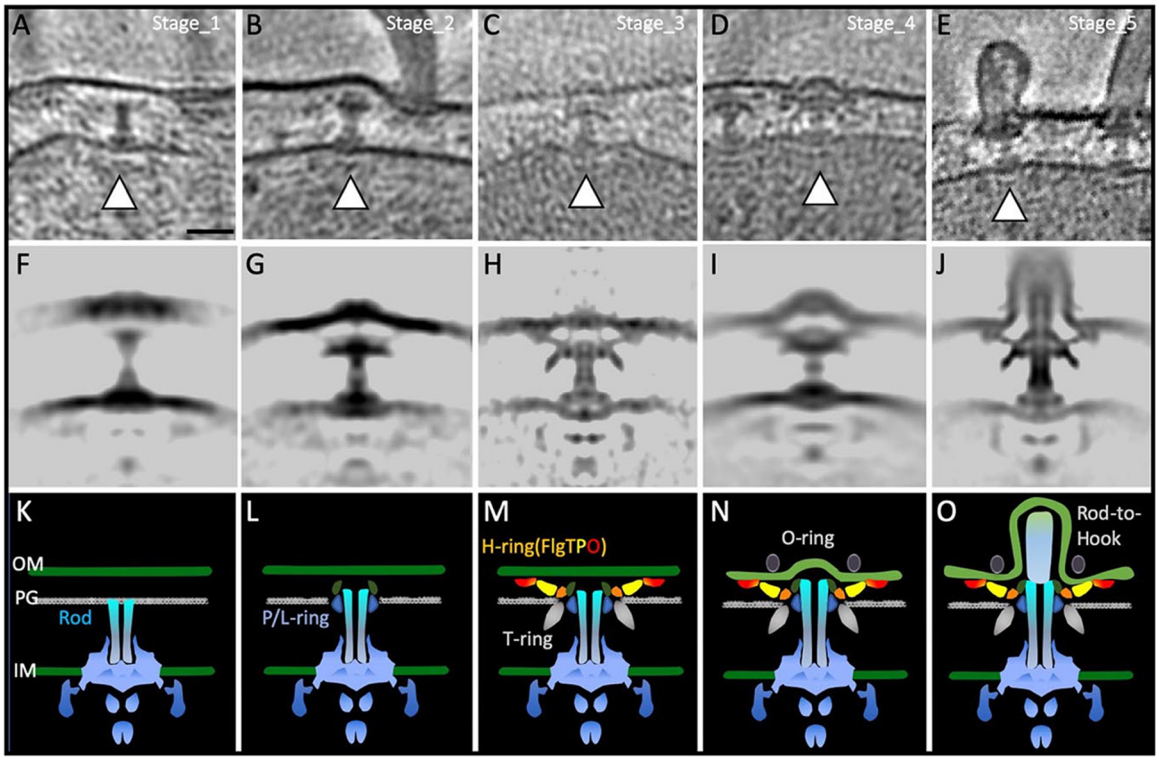

FIG 5 Flagellar ring formations captured by time coursed cryo-electron tomography. P/L rings assemble first, a *Vibrio*-specific T ring composed of MotX and MotY is next, and then FlgT, FlgP, and FlgO assemble to form the H ring. O-ring formation is now ready for the rod-hook transition. (A to E) Representative slice view of 3D tomograms showing different stages (from Stage_1 to Stage_5) during the flagellar assembly. (F to J) Central section of the subtomogram-averaged structure from different stages. (K to O) Cartoon models of structures shown in panels F to J. Bar, 20 nm.

intermediate states of the flagellar assembly process. We prepared fresh cultures of KK148 cells with multiple polar flagella and of VIO5 cells possessing single polar flagella. Cells were collected at time points of 20, 40, 80, and more than 180 min, and observed by cryo-ET (Fig. S4 and S5). Five significantly different basal body structures were obtained in the raw tomograms (Fig. 5A to J), which were named Stage_1 to Stage_5. The rod is constructed in the periplasm, but no bushing structure is formed in Stage_1, (Fig. 5A and F). In Stage_2, the P ring surrounds the rod (Fig. 5B and G). In Stage_3, the T-ring density appears around the P ring, and a partial density of the H ring is visible in raw tomograms (Fig. 5C and H). In Stage_4, the T ring and the H ring seem to be completed, the outer membrane begins to swell, and the O-ring density appears (Fig. 5D and I). In Stage_5, the hook grows in the sheath. Taking these findings together, we presented a plausible assembling sequence of the sheathed flagellum.

DISCUSSION

***Vibrio*-specific feature intimately associated with the L/P rings.** Our high-resolution cryo-ET map provided direct evidence that the T ring is composed of 26 units around the P ring. The density corresponding to FlgT in the H ring has a 26-fold rotational symmetry (Fig. 2A and C). The map resolved the subunits in the L/P rings of the *Vibrio* motor with 26-fold rotational symmetry, indicating that the L/P rings consist of 26 subunits of FlgH and FlgI, as shown for the L/P rings in the *Salmonella* flagellar motor (11). Both T/H rings are tightly associated with the L/P rings, presumably facilitating the interactions between the motor, the outer membrane, and the PG layer. Our new pseudoatomic model of the T/H rings enables us to appreciate the striking differences between the polar flagellar motor in *Vibrio* and the peritrichous flagellar motor in *Salmonella*.

Stator-rotor interaction triggers a large conformational change of the stator unit and an interaction between PomB and MotX. It is believed that the *Vibrio* stator is anchored to the PG layer through PomB, as suggested for the *Salmonella* motor (7), because the periplasmic region of PomB ($PomB_C$) has a conserved OmpA-like domain. Also, PomB directly interacts with the T ring through MotX, and the interaction is essential for proper incorporation of the stators into the motor (16, 18). The N-terminal disordered region in $PomB_C$ was expected to be responsible for interaction with the T ring (6). However, the high-resolution cryo-ET map with the superposition of the crystal structure of the $PomB_C$ dimer clearly shows that $PomB_C$ interacts with the tip of the T ring through the putative PG-binding site. It seems that $PomB_C$ does not directly interact with the PG layer. The structure of OmpA in complex with a PG analog (28) (PDB identifier [ID] 3TD5) and the structure of Pal bound to a PG precursor (29) (PDB ID 2AIZ), demonstrated that the PG-binding site of the OmpA-like domain interacts with the extended peptide region of PG but not with the sugar moiety. Thus, it would be possible that the minor differences in the PG-binding site enable $PomB_C$ to bind to an extended loop in MotX instead of to the PG peptide. It is also possible that the PG binding to $PomB_C$ occurs at the lateral surface of the OmpA-like domain, whose binding site is unmasked after the conformational change of $PomB_C$ to anchor around the motor, as suggested for the *Salmonella* motor (7). In this case, the stator units are anchored via not only the T ring but also the PG layer. Such a double anchoring system would reinforce the stator to power high-speed rotation.

In either case, the large conformational change of the stator is required to facilitate the interactions because the compact form of the stator is too short to reach the PG layer or the T ring. In fact, despite the observed strong interaction between $PomB_C$ and MotX in the intact motor, $PomB_C$ was unable to attach to the T ring in the absence of the rod and the MS ring. Therefore, the rotor-stator interaction is required to trigger the stator conformational change from a compact form to an extended form, as suggested previously (6, 27).

FOMC is composed of flagellar T/H/P/L rings without a stator ring. Recently several groups reported visualization of a flagellar basal body-like structure at the cell pole in polar-flagellated systems (10, 26, 30, 31). The structure was absent in *Pseudomonas aeruginosa* mutant cells lacking the flagellar rod protein and was designated FOMC (10). The FOMC as the bushing part of the flagellar motor would be the remnant of flagellar disassembly (10, 26). A pioneering study revealed that *Caulobacter* species eject a filament-hook-rod (FHR) complex when the cell differentiates from motile swimmer cells into sessile stalked cells (32, 33). In the basal body of the *Caulobacter* flagellum, the L/P rings would remain and embed in the outer membrane after FHR ejection. The L/P rings are nonrotating parts of the flagellar motor. We showed that the rod dysfunction mutant does not form an FOMC, suggesting that the FOMC observed previously is the structure formed by the ejection of FHR.

Our previous work revealed that FOMC structures exist in *Salmonella* species (10). Thus, FOMC would be a general product during flagellar disassembly. Similar FOMC structures are visible in the *Vibrio* hyperpolar sheathed flagellar system (Fig. 4). The loss of density of the FOMC in both *flgT* and *flgO* mutants is the same as that in the case of an intact motor structure in both mutants. The evidence supports the interpretation that FOMC is derived from the flagellar system and that the remaining structures result from ejection of FHR. While the 26 protrusions were clearly visible in the T-ring part of FOMC, no additional density was observed beneath the T ring (Fig. 4), indicating that no stator protein assembles around the FOMC. The interaction between the stator A subunit and the rotor is expected to trigger the structural change of the stator B subunit to anchor the stator (6). Since FOMC lacks the rotor, the stators cannot bind to the T ring of FOMC.

Time-coursed cryo-ET enabled us to visualize many distinct flagellar subassemblies. We captured the subassembly of the MS ring with the C ring, which is similar to the averaged structure of Δ*flgF* (Fig. 5; see Fig. S4 in the supplemental material). We

TABLE 2 Strains and plasmids used in this study

Strain or plasmid	Genotype or description[a]	Reference or source
Vibrio alginolyticus strains		
VIO5	Rif^r Pof$^+$ Laf$^-$	55
KK148	VIO5 *flhG* (Pof$^+$ Laf$^-$ multi-Pof)	56
NMB191	VIO5 Δ*pomAB* (Laf$^-$ Mot$^-$)	57
TH1	KK148 Δ*motX* (multi-Pof Laf$^-$ Mot$^-$)	16
TH2	KK148 Δ*motY* (multi-Pof Laf$^-$ Mot$^-$)	16
TH3	KK148 Δ*motXY* (multi-Pof Laf$^-$ Mot$^-$)	16
TH7	KK148 Δ*flgT* (multi-Pof Laf$^-$ Fla$^-$)	21
NMB300	KK148 Δ*pomAB* (multi-Pof Laf$^-$ Mot$^-$)	20
NMB337	KK148 Δ*flgO* (multi-Pof Laf$^-$ Fla$^-$)	9
NMB352	KK148 Δ$flgB_{C\ (51–124)}$ (multi-Pof Laf$^-$ Fla$^-$)	This study
NMB354	KK148 Δ$flgC_{C\ (56–130)}$ (multi-Pof Laf$^-$ Fla$^-$)	This study
NMB356	KK148 Δ$flgFc_{\ (118–242)}$ (multi-Pof Laf$^-$ Fla$^-$)	This study
NMB357	KK148 Δ$flgG_{N\ (8–140)}$ (multi-Pof Laf$^-$ Fla$^-$)	This study
Escherichia coli strains		
DH5α	F$^-$ ϕ80d*lacZ*ΔM15 Δ(*lacZYA-argF*)*U169 deoR recA1 endA1 hsdR17*(r_K^- m_K^+) *phoA supE44* λ$^-$ *thi-1 gyrA96 relA1*	58
S17-1	Tp^r Sm^r F$^-$ *recA thi pro hsdR RP4-2*(Tc::Mu-1 Km::Tn7) λpir	59
β3914	Km^r Em^r Tc^r *β2163 gyrA462 zei-298*::Tn*10*	36
Plasmids		
pBAD33	Cm^r P_{BAD}	60
pSU41	Km^r P_{lac}	61
pMMB206	Cm^r P_{tac} P_{lac} UV5	62
pSW7848	Exchange, oriVR6Kχ *oriTRP4 araC*-P_{BAD}-*ccdB*	63
pHFAB	*pomA* and *pomB* in pBAD33	64
pTSK155_2	Δ$flgB_{C\ (51–124)}$ in pSW7848	This study
pTSK157_2	Δ$flgC_{C\ (56–130)}$ in pSW7848	This study
pTSK160_2	Δ$flgF_{C\ (118–242)}$ in pSW7848	This study
pTSK161_2	Δ$flgG_{N\ (8–140)}$ in pSW7848	This study

[a]Rif^r, rifampin resistant; Km^r, kanamycin resistant; Cm^r, chloramphenicol resistant; Em^r, erythromycin resistant; Sm^r, streptomycin resistant; Tp^r, trimethoprim resistant; Tc^r, tetracycline resistant; Pof$^+$, normal polar flagellar formation; multi-Pof, multiple polar flagellar and/or basal body formation (hyperpolar flagella); Laf$^-$, lateral flagellar formation defect; Mot$^-$, motility defect; Fla$^-$, flagellar formation defect; P_{lac}, *lac* promoter; P_{tac}, *tac* promoter; P_{BAD}, arabinose promoter.

also captured the MS/C rings with the rod (Fig. 5A and F). The L/P rings were found to be coupled to flagellar rod polymerization (Fig. 5B and G). *Vibrio*-specific T/H/O rings assemble around the L/P rings (Fig. 5C, D, H, and I). Upon T/H ring complex completion, assembly transitions from rod to hook, which might be coupled to sheath formation with the help of the O ring (Fig. 5E and J). The hook acts as a ruler to sense its own length for transition to filament assembly (34, 35). After the basal body, which includes MS/C rings, rod, and P/L/T/H/O rings, is assembled, stator units are recruited and assembled around the rotor.

MATERIALS AND METHODS

Bacterial strains, plasmids, and growth condition. Bacterial strains used in this study are listed in Table 2. *V. alginolyticus* strains were cultured at 30°C in VC medium (0.5% [wt/vol] polypeptone, 0.5% [wt/vol] yeast extract, 3% [wt/vol] NaCl, 0.4% [wt/vol] K_2HPO_4, 0.2% [wt/vol] glucose) or VPG medium (1% [wt/vol] polypeptone, 3% [wt/vol] NaCl, 0.4% [wt/vol] K_2HPO_4, 0.5% [wt/vol] glycerol). If needed, chloramphenicol and L-arabinose were added at final concentrations of 2.5 μg/ml and 0.02% (wt/vol), respectively. *E. coli* cells were cultured at 37°C in LB medium (1% [wt/vol] Bacto tryptone, 0.5% [wt/vol] yeast extract, 0.5% [wt/vol] NaCl). If needed, chloramphenicol and ampicillin were added at final concentrations of 25 μg/ml and 100 μg/ml, respectively. Introduction of plasmids into *Vibrio* strains were conducted by electroporation, as described previously (36). To delete the *flg* genes in *V. alginolyticus*, the upstream and downstream regions of the gene were cloned into the suicide vector pSW7848, and homologous recombination to allow allelic exchange for gene deletion was performed as previously described (37).

Sample preparation for cryo-ET observation. *V. alginolyticus* strains were cultured overnight at 30°C in VC medium and diluted 100-fold with fresh VC medium and cultured at 30°C at 220 rpm. After 5 h, cells were collected, washed twice with TMN500 medium (50 mM Tris-HCl at pH 7.5, 5 mM glucose, 5 mM $MgCl_2$, and 500 mM NaCl) and finally diluted with TMN500 medium. Colloidal gold solution (10-nm diameter) was added to the diluted *Vibrio* samples to yield a 10-fold dilution and then deposited on a freshly glow discharged, holey carbon grid for 1 min. The grid was blotted with filter paper and rapidly plunge-frozen in liquid ethane in a homemade plunger apparatus, as described previously (38). The

samples of VIO5 and KK148 cells for time-coursed cryo-ET assay were prepared as described above. The optical densities at 600 nm (OD_{600}) at different time points were monitored to make a growth curve.

Cryo-ET data collection and image processing. The frozen-hydrated specimens of KK148 and relative mutants were transferred to a Titan Krios electron microscope (FEI) equipped with a 300-kV field emission gun and a direct electron detector (Gatan K2 Summit). The images were collected at a defocus near 0 μm using a Volta phase plate and an energy filter with a 20-eV slit. The data were acquired automatically with SerialEM software (39, 40). During data collection, the phase shift was monitored in the range of ~pi/3 to pi2/3; when the phase shift was out of this range, the next spot of the phase plate was switched to be charged for use. A total dose of 50 $e^-/Å^2$ was distributed among 35 tilt images covering angles from −51° to +51° at tilt steps of 3°. The starting tilting angle was +36° instead of 0°. For every single tilt series collection, the dose-fractionated mode was used to generate 8 to 10 frames per projection image. Collected dose-fractionated data were first subjected to the motion correction program to generate drift-corrected stack files (41–43). The stack files were aligned using gold fiducial markers, and volumes were reconstructed by the weighted back-projection method, using IMOD and TOMO3D software to generate tomograms (44, 45).

Subtomogram analysis with i3 packages. Bacterial flagellar motors were detected manually using the i3 program (46, 47). We selected two points on each motor, one point at the C-ring region and another near the flagellar hook. The orientations and geographic coordinates of selected particles were then estimated. In total, 3,020 subtomograms of *Vibrio* intact motors and 1,040 subtomograms of FOMC from KK148 cells were used for subtomogram averaging analysis. For the subtomogram averages from mutants, 20 subtomograms from Δ*flgT* were picked for the averaging process, and 423 subtomograms from KK148 Δ*pomAB* were picked and analyzed. For the structural comparison of mutants, all of the averaged structures were low-pass filtered to a resolution of 50 Å. The i3 tomographic package was used on the basis of the "alignment by classification" method with missing wedge compensation for generating the averaged structure of the motor, as described previously (38).

Three-dimensional visualization and modeling. Tomographic reconstructions were visualized using IMOD (44). University of California, San Francisco (UCSF) Chimera and UCSF ChimeraX software were used for three-dimensional (3D) surface rendering of subtomogram averages (48, 49). For the molecular modeling, the initial models of the FlgT monomer and the N-terminal and C-terminal domains of the MotY and PomBc5 dimer were built from their X-ray crystal structures (PDB ID 3W1E, 2ZF8, and 3WPW) with remodeling using Coot and Rosetta Relax application (50, 51). The initial model of MotX was built using the Robetta server (52). The structures were manually docked into the density map using UCSF Chimera. The MotX/MotY dimer structure was optimized using the Rosetta Relax application. Rigid body refinement was then performed using JiggleFit (53) in Coot. The final model was refined with the real-space refinement program in Phenix (54).

Data availability. The cryo-ET map has been deposited in the Electron Microscopy Data Bank (EMDB) under accession code EMD-21027, and the coordinate data containing the theoretical model of MotX are available from the corresponding authors on request.

SUPPLEMENTAL MATERIAL

Supplemental material is available online only.

SUPPLEMENTAL FILE 1, PDF file, 3.5 MB.

ACKNOWLEDGMENTS

We thank Akiko Abe for technical assistance and Kelly Hughes for critically reading the manuscript prior to submission.

This research was supported by grants-in-aid for scientific research from the Ministry of Education, Science and Culture of Japan (grant JP18K19293 to S.K.) and the Program for Leading Graduate Schools of the Japan Society for the Promotion of Science (grant JP17J11237 to T.N.). T.N. was supported in part by the Integrative Graduate Education and Research program of Nagoya University. S.Z. and J.L. were supported by grants GM107629 and R01AI087946 from the National Institutes of Health.

REFERENCES

1. Berg HC. 2003. The rotary motor of bacterial flagella. Annu Rev Biochem 72:19–54. https://doi.org/10.1146/annurev.biochem.72.121801.161737.
2. Macnab RM. 2003. How bacteria assemble flagella. Annu Rev Microbiol 57:77–100. https://doi.org/10.1146/annurev.micro.57.030502.090832.
3. Leake MC, Chandler JH, Wadhams GH, Bai F, Berry RM, Armitage JP. 2006. Stoichiometry and turnover in single, functioning membrane protein complexes. Nature 443:355–358. https://doi.org/10.1038/nature05135.
4. Fukuoka H, Wada T, Kojima S, Ishijima A, Homma M. 2009. Sodium-dependent dynamic assembly of membrane complexes in sodium-driven flagellar motors. Mol Microbiol 71:825–835. https://doi.org/10.1111/j.1365-2958.2008.06569.x.
5. Kojima S, Imada K, Sakuma M, Sudo Y, Kojima C, Minamino T, Homma M, Namba K. 2009. Stator assembly and activation mechanism of the flagellar motor by the periplasmic region of MotB. Mol Microbiol 73:710–718. https://doi.org/10.1111/j.1365-2958.2009.06802.x.
6. Zhu S, Takao M, Li N, Sakuma M, Nishino Y, Homma M, Kojima S, Imada K. 2014. Conformational change in the periplamic region of the flagellar stator coupled with the assembly around the rotor. Proc Natl Acad Sci U S A 111:13523–13528. https://doi.org/10.1073/pnas.1324201111.
7. Kojima S, Takao M, Almira G, Kawahara I, Sakuma M, Homma M, Kojima C, Imada K. 2018. The helix rearrangement in the periplasmic domain of the flagellar stator B subunit activates peptidoglycan binding and ion influx. Structure 26:590–598.e5. https://doi.org/10.1016/j.str.2018.02.016.
8. Qin Z, Lin WT, Zhu S, Franco AT, Liu J. 2017. Imaging the motility and

chemotaxis machineries in *Helicobacter pylori* by cryo-electron tomography. J Bacteriol 199:e00695-16. https://doi.org/10.1128/JB.00695-16.
9. Zhu S, Nishikino T, Hu B, Kojima S, Homma M, Liu J. 2017. Molecular architecture of the sheathed polar flagellum in *Vibrio alginolyticus*. Proc Natl Acad Sci U S A 114:10966–10971. https://doi.org/10.1073/pnas.1712489114.
10. Zhu S, Schniederberend M, Zhitnitsky D, Jain R, Galan JE, Kazmierczak BI, Liu J. 2019. *In situ* structures of polar and lateral flagella revealed by cryo-electron tomography. J Bacteriol 201:e00117-19. https://doi.org/10.1128/jb.00117-19.
11. Thomas DR, Francis NR, Xu C, DeRosier DJ. 2006. The three-dimensional structure of the flagellar rotor from a clockwise-locked mutant of *Salmonella enterica* serovar Typhimurium. J Bacteriol 188:7039–7048. https://doi.org/10.1128/JB.00552-06.
12. Beeby M, Ribardo DA, Brennan CA, Ruby EG, Jensen GJ, Hendrixson DR. 2016. Diverse high-torque bacterial flagellar motors assemble wider stator rings using a conserved protein scaffold. Proc Natl Acad Sci U S A 113:E1917–E1926. https://doi.org/10.1073/pnas.1518952113.
13. Chen S, Beeby M, Murphy GE, Leadbetter JR, Hendrixson DR, Briegel A, Li Z, Shi J, Tocheva EI, Muller A, Dobro MJ, Jensen GJ. 2011. Structural diversity of bacterial flagellar motors. EMBO J 30:2972–2981. https://doi.org/10.1038/emboj.2011.186.
14. Furuno M, Sato K, Kawagishi I, Homma M. 2000. Characterization of a flagellar sheath component of PF60 and its structural gene in marine *Vibrio*. J Biochem 127:29–36. https://doi.org/10.1093/oxfordjournals.jbchem.a022580.
15. Sjoblad RD, Emala CW, Doetsch RN. 1983. Bacterial flagellar sheaths: structures in search of a function. Cell Motil 3:93–103. https://doi.org/10.1002/cm.970030108.
16. Terashima H, Fukuoka H, Yakushi T, Kojima S, Homma M. 2006. The *Vibrio* motor proteins, MotX and MotY, are associated with the basal body of Na^+-driven flagella and required for stator formation. Mol Microbiol 62:1170–1180. https://doi.org/10.1111/j.1365-2958.2006.05435.x.
17. Kojima S, Shinohara A, Terashima H, Yakushi T, Sakuma M, Homma M, Namba K, Imada K. 2008. Insights into the stator assembly of the *Vibrio* flagellar motor from the crystal structure of MotY. Proc Natl Acad Sci U S A 105:7696–7701. https://doi.org/10.1073/pnas.0800308105.
18. Okabe M, Yakushi T, Homma M. 2005. Interactions of MotX with MotY and with the PomA/PomB sodium ion channel complex of the *Vibrio alginolyticus* polar flagellum. J Biol Chem 280:25659–25664. https://doi.org/10.1074/jbc.M500263200.
19. Terashima H, Li N, Sakuma M, Koike M, Kojima S, Homma M, Imada K. 2013. Insight into the assembly mechanism in the supramolecular rings of the sodium-driven *Vibrio* flagellar motor from the structure of FlgT. Proc Natl Acad Sci U S A 110:6133–6138. https://doi.org/10.1073/pnas.1222655110.
20. Zhu S, Nishikino T, Kojima S, Homma M, Liu J. 2018. The *Vibrio* H-ring facilitates the outer membrane penetration of the polar sheathed flagellum. J Bacteriol 200:e00387-18.
21. Terashima H, Koike M, Kojima S, Homma M. 2010. The flagellar basal body-associated protein FlgT is essential for a novel ring structure in the sodium-driven *Vibrio* motor. J Bacteriol 192:5609–5615. https://doi.org/10.1128/JB.00720-10.
22. Terashima H, Kawamoto A, Morimoto YV, Imada K, Minamino T. 2017. Structural differences in the bacterial flagellar motor among bacterial species. Biophys Physicobiol 14:191–198. https://doi.org/10.2142/biophysico.14.0_191.
23. Mittl PR, Schneider-Brachert W. 2007. Sel1-like repeat proteins in signal transduction. Cell Signal 19:20–31. https://doi.org/10.1016/j.cellsig.2006.05.034.
24. Sato K, Homma M. 2000. Multimeric structure of PomA, the Na^+-driven polar flagellar motor component of *Vibrio alginolyticus*. J Biol Chem 275:20223–20228. https://doi.org/10.1074/jbc.M002236200.
25. Yonekura K, Maki-Yonekura S, Homma M. 2011. The structure of the flagellar motor protein complex PomAB: implications for the torque-generating conformation. J Bacteriol 193:3863–3870. https://doi.org/10.1128/JB.05021-11.
26. Ferreira JL, Gao FZ, Rossmann FM, Nans A, Brenzinger S, Hosseini R, Wilson A, Briegel A, Thormann KM, Rosenthal PB, Beeby M. 2019. γ-Proteobacteria eject their polar flagella under nutrient depletion, retaining flagellar motor relic structures. PLoS Biol 17:e3000165. https://doi.org/10.1371/journal.pbio.3000165.
27. Kojima S, Nonoyama N, Takekawa N, Fukuoka H, Homma M. 2011. Mutations targeting the C-terminal domain of FliG can disrupt motor assembly in the Na^+-driven flagella of *Vibrio alginolyticus*. J Mol Biol 414:62–74. https://doi.org/10.1016/j.jmb.2011.09.019.
28. Park JS, Lee WC, Yeo KJ, Ryu KS, Kumarasiri M, Hesek D, Lee M, Mobashery S, Song JH, Kim SI, Lee JC, Cheong C, Jeon YH, Kim HY. 2012. Mechanism of anchoring of OmpA protein to the cell wall peptidoglycan of the gram-negative bacterial outer membrane. FASEB J 26:219–228. https://doi.org/10.1096/fj.11-188425.
29. Parsons LM, Lin F, Orban J. 2006. Peptidoglycan recognition by Pal, an outer membrane lipoprotein. Biochemistry 45:2122–2128. https://doi.org/10.1021/bi052227i.
30. Kaplan M, Ghosal D, Subramanian P, Oikonomou CM, Kjaer A, Pirbadian S, Ortega DR, Briegel A, El-Naggar MY, Jensen GJ. 2019. The presence and absence of periplasmic rings in bacterial flagellar motors correlates with stator type. Elife 8:e43487. https://doi.org/10.7554/eLife.43487.
31. Kaplan M, Subramanian P, Ghosal D, Oikonomou CM, Pirbadian S, Starwalt-Lee R, Mageswaran SK, Ortega DR, Gralnick JA, El-Naggar MY, Jensen GJ. 2019. *In situ* imaging of the bacterial flagellar motor disassembly and assembly processes. EMBO J 38:e100957. https://doi.org/10.15252/embj.2018100957.
32. Johnson RC, Walsh MP, Ely B, Shapiro L. 1979. Flagellar hook and basal complex of *Caulobacter crescentus*. J Bacteriol 138:984–989.
33. Kanbe M, Shibata S, Umino Y, Jenal U, Aizawa SI. 2005. Protease susceptibility of the *Caulobacter crescentus* flagellar hook-basal body: a possible mechanism of flagellar ejection during cell differentiation. Microbiology 151:433–438. https://doi.org/10.1099/mic.0.27386-0.
34. Cohen EJ, Hughes KT. 2014. Rod-to-hook transition for extracellular flagellum assembly is catalyzed by the L-ring-dependent rod scaffold removal. J Bacteriol 196:2387–2395. https://doi.org/10.1128/JB.01580-14.
35. Cohen EJ, Ferreira JL, Ladinsky MS, Beeby M, Hughes KT. 2017. Nanoscale-length control of the flagellar driveshaft requires hitting the tethered outer membrane. Science 356:197–200. https://doi.org/10.1126/science.aam6512.
36. Kawagishi I, Okunishi I, Homma M, Imae Y. 1994. Removal of the periplasmic DNase before electroporation enhances efficiency of transformation in a marine bacterium *Vibrio alginolyticus*. Microbiology 140:2355–2361. https://doi.org/10.1099/13500872-140-9-2355.
37. Le Roux F, Binesse J, Saulnier D, Mazel D. 2007. Construction of a *Vibrio splendidus* mutant lacking the metalloprotease gene *vsm* by use of a novel counterselectable suicide vector. Appl Environ Microbiol 73:777–784. https://doi.org/10.1128/AEM.02147-06.
38. Zhu S, Qin Z, Wang J, Morado DR, Liu J. 2017. *In situ* structural analysis of the spirochetal flagellar motor by cryo-electron tomography. Methods Mol Biol 1593:229–242. https://doi.org/10.1007/978-1-4939-6927-2_18.
39. Mastronarde DN. 2005. Automated electron microscope tomography using robust prediction of specimen movements. J Struct Biol 152:36–51. https://doi.org/10.1016/j.jsb.2005.07.007.
40. Mastronarde DN, Held SR. 2017. Automated tilt series alignment and tomographic reconstruction in IMOD. J Struct Biol 197:102–113. https://doi.org/10.1016/j.jsb.2016.07.011.
41. Li X, Mooney P, Zheng S, Booth CR, Braunfeld MB, Gubbens S, Agard DA, Cheng Y. 2013. Electron counting and beam-induced motion correction enable near-atomic-resolution single-particle cryo-EM. Nat Methods 10:584–590. https://doi.org/10.1038/nmeth.2472.
42. Morado DR, Hu B, Liu J. 2016. Using Tomoauto: a protocol for high-throughput automated cryo-electron tomography. J Vis Exp 107:e53608. https://doi.org/10.3791/53608.
43. Zheng SQ, Palovcak E, Armache JP, Verba KA, Cheng Y, Agard DA. 2017. MotionCor2: anisotropic correction of beam-induced motion for improved cryo-electron microscopy. Nat Methods 14:331–332. https://doi.org/10.1038/nmeth.4193.
44. Kremer JR, Mastronarde DN, McIntosh JR. 1996. Computer visualization of three-dimensional image data using IMOD. J Struct Biol 116:71–76. https://doi.org/10.1006/jsbi.1996.0013.
45. Agulleiro JI, Fernandez JJ. 2015. Tomo3D 2.0—exploitation of advanced vector extensions (AVX) for 3D reconstruction. J Struct Biol 189:147–152. https://doi.org/10.1016/j.jsb.2014.11.009.
46. Winkler H. 2007. 3D reconstruction and processing of volumetric data in cryo-electron tomography. J Struct Biol 157:126–137. https://doi.org/10.1016/j.jsb.2006.07.014.
47. Winkler H, Zhu P, Liu J, Ye F, Roux KH, Taylor KA. 2009. Tomographic subvolume alignment and subvolume classification applied to myosin V and SIV envelope spikes. J Struct Biol 165:64–77. https://doi.org/10.1016/j.jsb.2008.10.004.
48. Pettersen EF, Goddard TD, Huang CC, Couch GS, Greenblatt DM, Meng EC, Ferrin TE. 2004. UCSF Chimera—a visualization system for explor-

atory research and analysis. J Comput Chem 25:1605–1612. https://doi.org/10.1002/jcc.20084.
49. Goddard TD, Huang CC, Meng EC, Pettersen EF, Couch GS, Morris JH, Ferrin TE. 2018. UCSF ChimeraX: meeting modern challenges in visualization and analysis. Protein Sci 27:14–25. https://doi.org/10.1002/pro.3235.
50. Emsley P, Lohkamp B, Scott WG, Cowtan K. 2010. Features and development of Coot. Acta Crystallogr D Biol Crystallogr 66:486–501. https://doi.org/10.1107/S0907444910007493.
51. Nivon LG, Moretti R, Baker D. 2013. A Pareto-optimal refinement method for protein design scaffolds. PLoS One 8:e59004. https://doi.org/10.1371/journal.pone.0059004.
52. Kim DE, Chivian D, Baker D. 2004. Protein structure prediction and analysis using the Robetta server. Nucleic Acids Res 32:W526–W531. https://doi.org/10.1093/nar/gkh468.
53. Brown A, Long F, Nicholls RA, Toots J, Emsley P, Murshudov G. 2015. Tools for macromolecular model building and refinement into electron cryo-microscopy reconstructions. Acta Crystallogr D Biol Crystallogr 71:136–153. https://doi.org/10.1107/S1399004714021683.
54. Adams PD, Afonine PV, Bunkoczi G, Chen VB, Davis IW, Echols N, Headd JJ, Hung LW, Kapral GJ, Grosse-Kunstleve RW, McCoy AJ, Moriarty NW, Oeffner R, Read RJ, Richardson DC, Richardson JS, Terwilliger TC, Zwart PH. 2010. PHENIX: a comprehensive Python-based system for macromolecular structure solution. Acta Crystallogr D Biol Crystallogr 66:213–221. https://doi.org/10.1107/S0907444909052925.
55. Okunishi I, Kawagishi I, Homma M. 1996. Cloning and characterization of *motY*, a gene coding for a component of the sodium-driven flagellar motor in *Vibrio alginolyticus*. J Bacteriol 178:2409–2415. https://doi.org/10.1128/jb.178.8.2409-2415.1996.
56. Kusumoto A, Kamisaka K, Yakushi T, Terashima H, Shinohara A, Homma M. 2006. Regulation of polar flagellar number by the *flhF* and *flhG* genes in *Vibrio alginolyticus*. J Biochem 139:113–121. https://doi.org/10.1093/jb/mvj010.
57. Yorimitsu T, Sato K, Asai Y, Kawagishi I, Homma M. 1999. Functional interaction between PomA and PomB, the Na^+-driven flagellar motor components of*Vibrio alginolyticus*. J Bacteriol 181:5103–5106.
58. Grant SG, Jessee J, Bloom FR, Hanahan D. 1990. Differential plasmid rescue from transgenic mouse DNAs into *Escherichia coli* methylation-restriction mutants. Proc Natl Acad Sci U S A 87:4645–4649. https://doi.org/10.1073/pnas.87.12.4645.
59. Simon R, Priefer U, Puhler A. 1983. A broad host range mobilization system for in vivo genetic engineering: transposon mutagenesis in Gram negative bacteria. Nat Biotechnol 1:784–791. https://doi.org/10.1038/nbt1183-784.
60. Guzman LM, Belin D, Carson MJ, Beckwith J. 1995. Tight regulation, modulation, and high-level expression by vectors containing the arabinose pBAD promoter. J Bacteriol 177:4121–4130. https://doi.org/10.1128/jb.177.14.4121-4130.1995.
61. Bartolome B, Jubete Y, Martínez E, de la Cruz F. 1991. Construction and properties of a family of pACYC184-derived cloning vectors compatible with pBR322 and its derivatives. Gene 102:75–78. https://doi.org/10.1016/0378-1119(91)90541-i.
62. Morales BM, Backman A, Bagdasarian M. 1991. A series of wide-host-range low-copy-number vectors that allow direct screening for recombinants. Gene 97:39–47. https://doi.org/10.1016/0378-1119(91)90007-X.
63. Val ME, Skovgaard O, Ducos-Galand M, Bland MJ, Mazel D. 2012. Genome engineering in *Vibrio cholerae*: a feasible approach to address biological issues. PLoS Genet 8:e1002472. https://doi.org/10.1371/journal.pgen.1002472.
64. Fukuoka H, Yakushi T, Kusumoto A, Homma M. 2005. Assembly of motor proteins, PomA and PomB, in the Na^+-driven stator of the flagellar motor. J Mol Biol 351:707–717. https://doi.org/10.1016/j.jmb.2005.06.037.